Thermodynamic properties of $MgSiO_3$ at super-Earth mantle conditions

D. E. Fratanduono,[1,*] M. Millot,[1] R. G. Kraus,[1] D. K. Spaulding,[2] G. W. Collins,[3] P. M. Celliers,[1] and J. H. Eggert[1]

[1]*Lawrence Livermore National Laboratory, Livermore, California 94550, USA*

[2]*Department of Earth and Planetary Sciences, University of California, Davis, California 95616, USA*

[3]*Laboratory for Laser Energetics, University of Rochester, Rochester, New York 14623, USA*

(Received 13 April 2017; revised manuscript received 29 May 2018; published 21 June 2018)

Recent discoveries of terrestrial exoplanets distant from our solar system motivate laboratory experiments that provide insight into their formation and thermal evolution. Using laser-driven shock wave experiments, we constrain high-temperature and high-pressure adiabats and the equation of state of $MgSiO_3$, a dominant mantle constituent of terrestrial exoplanets. Critical to the development of a habitable exoplanet is the early thermal history, specifically the formation and freezing of the magma ocean and its role in enabling convection in the mantle and core. We measure the adiabatic sound speed and constrain the melt transition along the Hugoniot and find that the adiabats and melt boundary of silicate magmas are shallower than predicted. This suggests that small changes in the temperature of a super-Earth mantle would result in rapid melting and solidification of nearly the entire mantle.

DOI: 10.1103/PhysRevB.97.214105

I. INTRODUCTION

The discovery of a large number of terrestrial "super-Earth" exoplanets sparked a renewed interest in the understanding of the fundamental properties of key planetary constituent materials, which in turn triggered unexpected findings. Shock compression studies on SiO_2 [1,2] and MgO [3–5] revealed that mantle minerals become electrically conductive in the fluid phase and could contribute to dynamo generation. They also point to enhanced specific heat in the fluid that may be due to complex polymerization phenomena [1–3]. Combining static and shock compression data on $MgSiO_3$ also suggests that the Grüneisen parameter of dense silicate fluid decreases with increasing volume [6], potentially due to changes in the liquid coordination.

Another study [7] reported the existence of a phase transformation to a low-entropy, high-density fluid phase of $MgSiO_3$ above 300–400 GPa and 10 000–16 000 K, based on the observation of simultaneous velocity and thermal-emission jumps along the decay of unsupported shock waves launched in both enstatite crystals and $MgSiO_3$ glass. Such a transition is not expected from state-of-the-art density functional theory molecular dynamics (DFT-MD) simulations [8] and a recent study using the same technique as Spaulding *et al.* [7] did not observe any thermal or velocity anomaly along the Hugoniot (locus of shock end states) of $MgSiO_3$ glass [5].

Here we report shock compression experiments on $MgSiO_3$ enstatite crystals, yielding measurements of the adiabatic sound speed, the shock temperature-pressure-density equation of state (EOS), and the Grüneisen parameter of dense fluid $MgSiO_3$. These measurements indicate that melting along the enstatite Hugoniot is complete at 227 (±10) GPa and 5745 (±530 K). Altogether, our thermodynamic property data indicate that the melting curve and the isentropes in the fluid are shallower than expected based on DFT-MD simulations, and are nearly parallel, which has important implications for the structure and evolution of terrestrial exoplanets, and in particular the fate of their primordial magma ocean.

The paper is outlined as follows. In Sec. II, we discuss the experimental technique used to determine the sound speed of liquid $MgSiO_3$ followed by a discussion of the Hugoniot measurements in Sec. III. In Sec. IV, we discuss the calculation of the Grüneisen parameter using our sound speed and Hugoniot determination. Following this, we discuss optical measurements of the solid phases within Sec. V and thermal-emission measurements of the shock front in Sec. VI. Finally in Sec. VII, we combine the measurements from Secs. II–VI to develop a better understanding of liquid $MgSiO_3$ and the implications for terrestrial "super Earths."

II. SOUND SPEED MEASUREMENTS

The shock compression experiments were performed at the OMEGA laser facility [1], using up to 12 laser beams with up to 1.78 kJ of 351 nm UV light to launch strong shock waves in a planar target package by direct-drive ablation. SG8 distributed phase plates created a super-Gaussian illumination profile having an ~800 μm diameter. The planar target (see Fig. 1) consisted of a $MgSiO_3$ sample and a quartz witness plate affixed side-by-side to a common quartz drive plate, mounted on a 27 μm ablator/Au preheat shield package.

An electron microprobe analysis of the enstatite crystals was performed to determine the chemical composition. Samples were cut with the c axis perpendicular/normal to the surface. The results are shown in Table I. Prior to dicing the sample, the enstatite density was measured using the Archimedes

*Author to whom correspondence and requests for materials should be requested: Fratanduono1@llnl.gov

 ©2018 American Physical Society

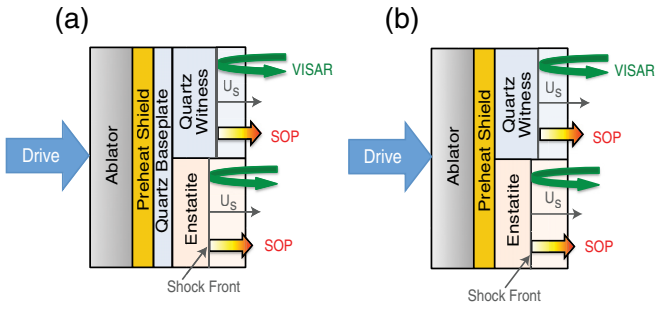

FIG. 1. Experimental target design. (a) Target design used for sound speed measurements. (b) Target design used in the decaying shock wave experiments. Layers are not drawn to scale.

principle. The sample density was determined to be 3.212(±0.002) g/cc.

Carefully tailored 7.6-ns-long laser pulses launched quasisteady shock waves into the target stacks that were strong enough to transform the shock compressed quartz and $MgSiO_3$ into optically reflecting states so that the two-channel, ultrafast velocimeter interferometer system for any reflector (VISAR) tracked the shock waves as they propagated (Fig. 2). Superimposing small fluctuations to the drive laser pulse shape created small acoustic perturbations that travel in the shock compressed materials. These fluctuations overtake the leading shock wave resulting in small modulations of the observed shock velocity. Figure 2 illustrates that these velocity modulations appear shifted in time and dilated in amplitude in the enstatite sample, compared to the modulations observed in the quartz witness.

By relying on the knowledge of the sound speed and of the pressure-density compressibility of shock compressed quartz [9], the $MgSiO_3$ sound speed can be determined by a linear-scaling analysis [10] using the experimental measurements of the relative speed of the acoustic perturbations to catch up with the leading shock front $\frac{\Delta t_S}{\Delta t_R}$ (see Fig. 1).

For quasisteady shock waves with small acoustic perturbations ($\frac{\Delta P}{P} < 10\%$), the acoustic perturbations at the shock front are related to the perturbations at a source though a linear scaling of parameters (these concepts are discussed in detail within Fratanduono *et al.* [10]). For multisection targets that experience a common drive, the Doppler shift and the perturbation amplitudes for adjacent regions are related through linear scaling parameters. Consider a target which consists of a witness and sample affixed to a common baseplate [see Fig. 1(a)]. Each section of that target observes a common quasisteady pressure source. Fluctuations in the pressure drive are observed as modulations in the shock-front amplitudes and as Doppler shifts in the arrival time by scaling parameters. If the perturbation arrival time scaling factor ($\frac{\Delta t_S}{\Delta t_R}$) is measured and the EOS of the witness is known, the sample sound speed

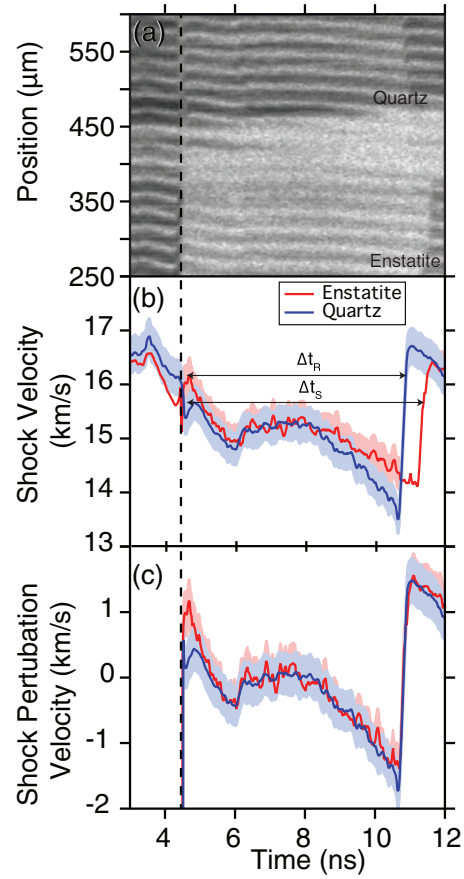

FIG. 2. Typical VISAR data obtained in order to determine the $MgSiO_3$ sound speed is shown. (a) The raw VISAR data illustrating a two-section target where the shock velocity in a quartz witness and $MgSiO_3$ sample are measured simultaneously. (b) The shock-front velocity determined from (a). (c) By mapping the fluctuations from the $MgSiO_3$ sample onto the quartz witness, we determine out perturbations within the witness are Doppler shifted in the sample, enabling extraction of the sample sound speed. The relative difference in the Doppler shift ($\frac{\Delta t_S}{\Delta t_R}$) determines the $MgSiO_3$ Eulerian sound speed.

is determined from

$$C_s = \frac{P_S}{U_{p,S}\rho_S}\left(1 - \frac{(1 - M_{S1,d})(1 + M_{R1,d})}{\frac{\Delta t_S}{\Delta t_R}(1 + M_{R1,u})}\right)^{-1}, \quad (1)$$

where Δt_S and Δt_R are the difference in the arrival times at the sample and reference shock front, respectively, for a fixed set of perturbations, P_S is the sample shock pressure, $U_{p,S}$ is the sample particle velocity, ρ_S is the sample density, M is the mach number ($M = \frac{U_f}{C_s}$) which represents the ratio of wave-front speed (U_f) to the local sound speed, $M_{S1,d}$ is the witness downstream shock-front Mach number, $M_{R1,u}$ is the baseplate upstream Mach number, and $M_{R1,d}$ is the baseplate

TABLE I. Oxide weight percents obtained by electron microprobe analysis.

Sample	SiO_2	TiO_2	Al_2O_3	Cr_2O_3	FeO	MnO	MgO	CaO	NiO	Total
Enstatite	59.00(±0.04)	B.D.L.[a]	1.51(±0.01)	B.D.L.	0.41(±0.03)	B.D.L.	38.96(±0.08)	0.06(±0.02)	B.D.L.	100.00

[a]Below detection limit (B.D.L.).

TABLE II. Enstatite Eulerian sound speed and Grüneisen measurements.

Shot number	U_s^{quartz} (km/s)	U_s (km/s)	U_p (km/s)	P (GPa)	ρ (g/cc)	$\frac{\Delta t_R}{\Delta t_S}$ (unitless)	C_s (km/s)	Γ (unitless)
s75633B	12.3(±0.2)	12.6(±0.2)	5.8(±0.1)	237(±6)	6.0(±0.2)	0.90(±0.01)	12.0(±0.4)	0.88(±0.2)
s75634A	13.7(±0.2)	14.1(±0.2)	6.7(±0.2)	304(±8)	6.2(±0.2)	0.90(±0.01)	13.2(±0.5)	0.88(±0.2)
s75636A	14.4(±0.2)	14.5(±0.2)	7.2(±0.2)	335(±8)	6.4(±0.2)	0.90(±0.01)	13.1(±0.5)	0.96(±0.2)
s75636B	14.3(±0.2)	14.4(±0.2)	7.1(±0.2)	330(±8)	6.4(±0.2)	0.90(±0.01)	13.2(±0.5)	0.93(±0.2)
s75637A	15.3(±0.2)	15.3(±0.2)	7.8(±0.2)	384(±9)	6.6(±0.2)	0.92(±0.01)	13.6(±0.5)	0.95(±0.2)
s75640A	13.5(±0.2)	13.5(±0.2)	6.7(±0.2)	290(±8)	6.4(±0.2)	0.90(±0.01)	12.3(±0.5)	0.97(±0.2)
s75640B	13.2(±0.2)	13.5(±0.2)	6.4(±0.2)	276(±7)	6.1(±0.2)	0.90(±0.01)	12.7(±0.5)	0.87(±0.2)

downstream Mach number. Provided that the mechanical EOS of the witness and baseplate are known, $M_{R1,u}$,$M_{R1,d}$, and $M_{S1,d}$ are known.

In this work, we utilized a quartz reference due to the recent work of Knudson and Desjarlais developing quartz as a standard [9]. To determine the sample sound speed, the principal Hugoniot is required. For enstatite single crystals, we performed a fit to all available Hugoniot data [7,11,12]. A Levenberg-Marquardt nonlinear least-squares optimization routine was used to determine the linear scaling parameter that maps the sample shock velocity onto the witness shock velocity. The measured enstatite Eulerian sound speeds are provided in Table II.

Seven experiments between 237 and 384 GPa provide measurements of the Eulerian sound speed ($\sqrt{\frac{dP}{d\rho}|_S}$) of fluid $MgSiO_3$ along the enstatite principal Hugoniot (Fig. 3). Our sound speed measurements increase monotonically over the explored pressure range, contradicting the existence of a strong density, compressibility, and entropy jump along the enstatite near 300 GPa as proposed in Ref. [7].

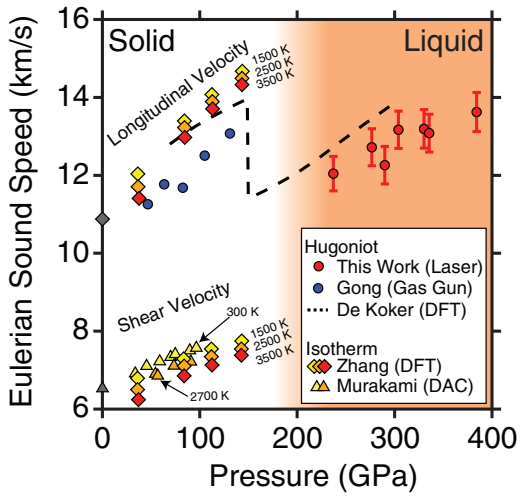

FIG. 3. Eulerian sound speed measurements (red points) along the $MgSiO_3$ principal Hugoniot are compared with DFT principal Hugoniot calculations [15] (black dashed line), gas-gun Hugoniot sound speed measurements [13] (blue circles), DAC measurements [14], and theoretical isentropic bulk velocities and isentropic shear velocities [16]. The reduction in sound speed of these measurements, when compared to the DAC data [13] are indicative of a loss in shear strength due to melt.

Comparing our measurements in Fig. 3 (red circles) with previous lower-pressure shock measurements [13] (blue circles) as well as static compression data [14] (colored triangles) shows that our data are higher than the shear wave sound speed measurement but lower than the longitudinal sound speed in the solid, consistent with a loss in shear strength due to melt. The measurement bound the onset and completion of melt along the Hugoniot between 140 GPa (highest shock datum from Ref. [13]) and 237 GPa (lowest datum of this work). Our data are also of slightly lower sound speed than the predictions from density functional theory (DFT) simulations along the enstatite Hugoniot [15] (black dashed line).

III. HUGONIOT MEASUREMENTS

Impedance match data to a quartz standard [9] was a by-product of our sound speed experiments. By measuring the shock-velocity history, we characterized the shock-velocity discontinuity upon the transmission of the shock through the quartz baseplate–$MgSiO_3$ sample interface, from which we obtained pressure-density shock compressibility. We obtained the shock Hugoniot response (U_s-U_p) through impedance matching [9,17] of the shock-velocity change as the shock traversed the quartz/MgSiO3 interface.

The sound speed experimental design required the use of acoustic perturbations. As a result, the technique precluded the use of steady shock waves, resulting in large uncertainties in the quartz and enstatite shock velocities used in the impedance matching analysis (e.g., these experiments were not optimized to produce high-quality Hugoniot data). Regardless, these results (included in Table III) were found to be in agreement with a linear extrapolation of the low-pressure gas-gun data [11,12].

Since this work did not reproduce the observations of Spaulding *et al.* [7] suggesting a volume change in the liquid and a discontinuity in the principal Hugoniot, the raw experimental equation of state data measured by Spaulding *et al.* [7] from the OMEGA facility was reanalyzed (the JANUS data was not revisited due to data quality concerns). In their original analysis, systematic uncertainties in the treatment of epoxy layers in the impedance matching analysis as well as systematic uncertainties in the phase determination were found and corrected. These corrections, coupled with the most recent quartz reference model [9] show that this data no longer supports a discontinuity in the principal Hugoniot, as a linear fit represents the data well (the corrected values are provided in Table III). As a result, in this work we utilized a linear fit to all available enstatite Hugoniot data [7,11,12].

TABLE III. Equation of state data for $MgSiO_3$.

Starting material	Shot	U_s^{quartz} (km/s)	$U_s^{MgSiO_3}$ (km/s)	$U_p^{MgSiO_3}$ (km/s)	P^{MgSiO_3} (GPa)	ρ^{MgSiO_3} (g/cc)
Single crystal	s75633	12.46(±0.17)	12.62(±0.23)	6.00(±0.31)	243(±13)	6.12(±0.32)
Single crystal	s75640	13.39(±0.28)	13.64(±0.31)	6.57(±0.36)	288(±16)	6.19(±0.38)
Single crystal	s75636	15.11(±0.20)	14.84(±0.21)	7.75(±0.34)	370(±16)	6.73(±0.35)
Single crystal	s75634	15.28(±0.17)	15.14(±0.40)	7.84(±0.33)	381(±17)	6.66(±0.40)
Single crystal	s75637	15.42(±0.23)	16.01(±0.15)	7.81(±0.35)	401(±18)	6.27(±0.28)
Single crystal	s75635	16.08(±0.29)	16.19(±0.25)	8.33(±0.38)	433(±20)	6.61(±0.36)
Single crystal[a]	CEOS1	19.70(±0.30)	20.00(±0.20)	10.8(±0.25)	691(±17)	7.04(±0.21)
Single crystal[a]	CEOS2	21.20(±0.20)	21.10(±0.20)	11.9(±0.25)	808(±18)	7.39(±0.22)

[a]Reanalysis of the two OMEGA experiments conducted by Spaulding *et al.* [7].

We find that a linear fit represents these data well as shown in Fig. 4. The revised Hugoniot for crystalline enstatite used is $U_s[\text{km/s}] = 4.75(\pm0.03) + 1.37(\pm0.01)U_p[\text{km/s}]$.

IV. GRÜNEISEN CALCULATION

Using these sound speed measurements and the pressure-density compressibility along the Hugoniot, we compute [18] the Grüneisen parameter (Γ), which determines the adiabatic temperature profile. The Grüneisen parameter was determined from the principal Hugoniot and the relation [18]

$$\Gamma = \frac{2}{\rho}\frac{C_s^2\rho^2 - \rho^2\frac{dP}{d\rho}|_{\text{Hug}}}{P - \rho^2\frac{dP}{d\rho}|_{\text{Hug}}\left(\frac{1}{\rho_0} - \frac{1}{\rho}\right)}, \tag{2}$$

where P is the Hugoniot pressure, ρ is the Hugoniot density, ρ_0 is the initial sample density, C_s is the Eulerian sound speed, and $\frac{dP}{d\rho}|_{\text{Hug}}$ is the local pressure derivative with respect to density along the principal Hugoniot. Over this pressure range, we find an average value of $\Gamma = 0.92 \pm 0.08$ slightly smaller than DFT [15]. Our data thus suggest that the temperature rise with increasing pressure and density along isentropes in dense $MgSiO_3$ fluid is slower than predicted using DFT.

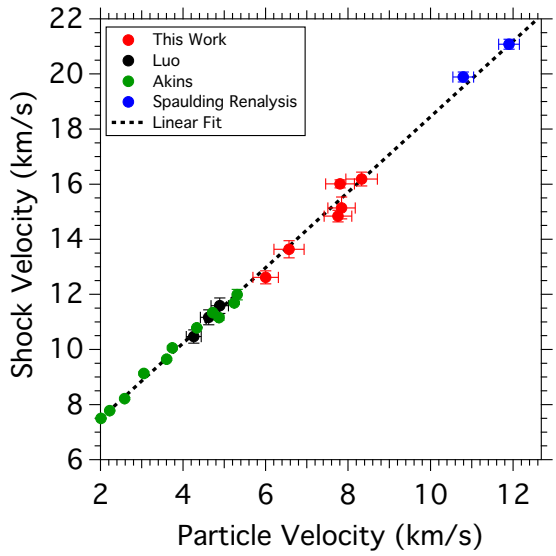

FIG. 4. Experimentally determined enstatite principal Hugoniot data are shown. The experimental measurements from this work are shown as red circles, Luo *et al.* [11] as black circles, Akins *et al.* [12] as green circles, and a reanalysis of the Spaulding *et al.* [7] as the blue circles. We find that a linear fit represents these data and the linear U_s-U_p fit is shown as the black dashed line.

V. ENSTATITE OPTICAL PROPERTIES

Two experiments were performed to investigate the transparency of enstatite within the solid phase (see Fig. 1(a). The VISAR diagnostic measured the shock velocity within the quartz baseplate and the apparent enstatite particle velocity (U_{App}). Here, we used the refractive index of pristine enstatite and quartz $n_{\text{Ens}} = 1.66$ and $n_{\text{quartz}} = 1.547$ to obtain the true shock velocity from the apparent VISAR velocity [19]. The shocked refractive index is defined as

$$n_s = \frac{U_{\text{App}} - U_s n_0}{U_p - U_s}, \tag{3}$$

where U_s is the enstatite shock velocity, n_0 is the enstatite ambient refractive index (1.66 ± 0.01), and U_p is the enstatite particle velocity. The refractive index measurements from this work are provided in Table IV. To determine the enstatite shock velocity and particle velocity, impedance matching between the quartz shock velocity and enstatite sample was performed. The quartz release model of Knudson *et al.* [9] is not calibrated over the low-pressure range of these experiments and we used the reflected quartz Hugoniot as an approximation for impedance matching [9].

A linear fit to the refractive index versus density was performed and found to be

$$n_s = 1.45(\pm0.10) + 0.070(\pm0.026)\rho. \tag{4}$$

Since the shock was decaying in both the quartz and the enstatite sample, the absorption length within the enstatite could not be determined. We found that $MgSiO_3$ remained transparent to 164 (±7) GPa (highest pressure measurement performed) in agreement with previous measurements [11] showing that the absorption depth of $MgSiO_3$ along the enstatite Hugoniot is large (~25 μm at ~650 nm and at ~190 GPa) in the solid phase. As previously shown, upon melting, transparent insulators transition to opaque materials due to closing of the band gap [20]. Our transparency measurements therefore also provide an additional lower bound on the melt transition [$P_{\text{melt}} > 164(\pm7)$ GPa].

TABLE IV. Enstatite refractive index measurements.

Shot number	Quartz U_s (km/s)	Enstatite U_{App}	Enstatite U_s (km/s)	Enstatite U_p (km/s)	Enstatite P (GPa)	Enstatite ρ (g/cc)	Enstatite n_s
s79479	8.67(±0.14)	5.10(±0.17)	9.29(±0.52)	3.60(±0.11)	108(±5)	5.28(±0.26)	1.813(±0.069)
s79480	10.42(±0.12)	6.63(±0.15)	11.10(±0.56)	4.61(±0.12)	164(±7)	5.53(±0.29)	1.816(±0.066)

VI. TEMPERATURE MEASUREMENTS

We also conducted decaying shock experiments similar to the ones previously reported [5,7] to measure the variation of the thermal emission as a function of shock velocity. In these experiments, a 1 ns square pulse of ~200 to ~800 J generated strong but unsupported shocks that decayed in amplitude as they traveled through a planar target package having a 50 μm ablator, a 2 μm Au preheat shield, and a single-crystal enstatite sample side-by-side with a quartz witness sample [Fig. 1(b)]. Both the $MgSiO_3$ sample and the quartz witness free surface were coated with a 532 nm antireflection coating to prevent ghost reflections. The shock velocity and thermal emission were spatially and temporally resolved using the VISAR and a streaked optical pyrometer (SOP), respectively [1,2] (see Fig. 5). Through temporal calibration of the two instruments, a continuous measure of the thermal emission as a function of the shock velocity was obtained to infer the evolution of the shock temperature as a function of pressure [1,2] along the enstatite Hugoniot.

Using the shock compressibility U_s-U_p relationship determined here and the Rankine-Hugoniot equations allows us to convert U_S into shock pressure. SOP counts were converted into shock temperature T using a gray-body approximation, the shock-front reflectivity R to obtain the emissivity $\epsilon = 1 - R$, and the quartz witness as a temperature calibration standard [1,2,17], so that we obtained temperature vs pressure measurements for five decaying-shock experiments. The average of those shots is shown in Fig. 8.

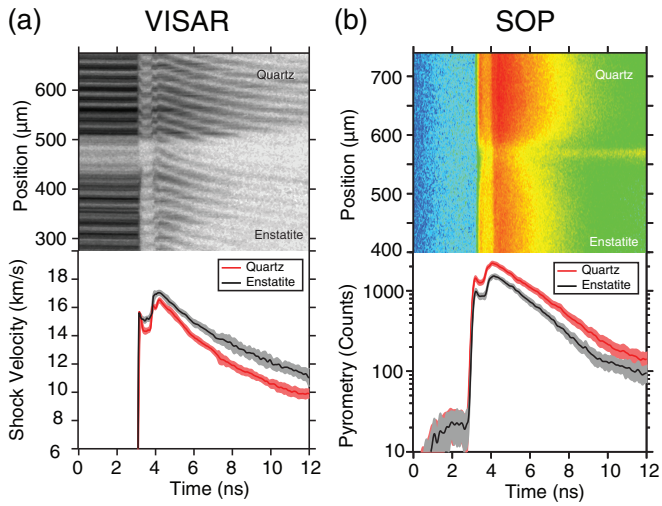

FIG. 5. The experimental VISAR and SOP data from a single experiment (s77778). (a) The experimental raw (top) and analyzed (bottom) spatially resolved shock-velocity data. The VISAR diagnostic produces a sinusoidal spatial modulation on the image where Doppler shifts in a probe laser reflected off of the shock front appear as displacement of the fringes record in the streak record. The displacement of these fringes is directly related to the shock velocity. (b) The experimental raw (top) and analyzed (bottom) spatially resolved thermal emission from the shock front. A change in the thermal-emission decay slope of the enstatite sample is observed at ~9.3 ns and is not observed in the quartz witness.

In this work, we find no evidence of the phase transformation at ~300 GPa as previously proposed [7]. Four decaying shock experiments were performed at the OMEGA laser facility to reproduce the previous results. In the present work, a significant modification in the target design [see Fig. 1(b)] was the use of a two-section target that consisted of an enstatite sample and a quartz witness. The quartz witness served to ensure that any acoustic perturbations in the decaying shock velocity common to both sections of the target were not interpreted as phase-transition signatures and to provide an *in situ* temperature calibrant.

Since we found no evidence of the proposed liquid-liquid phase transition, we reinvestigated the simultaneous velocity and thermal emission jumps shown by Ref. [7]. When the shock-velocity and thermal-emission observables are compared it is found that the proposed anomaly tracks the same shock velocity/shock temperature path, as might be expected for an acoustic perturbation. The most likely mechanism for the previous observations may be an acoustic perturbation in the target; however, this cannot be definitively verified. Hydrocode simulations of the targets used in [7] do not suggest that such a perturbation should have been present given the experimental design; however, unexpected deviations in the laser pulse shape could be capable of producing such effects. Laser pulse-shape histories were not available for the previous experiments and similar signatures were not observed in identical target packages with other sample materials.

Furthermore, a 2000 K difference in shock temperature was recorded in these experiments attributed to recent improvements to the diagnostic temporal resolution, calibration, and system response, while similar shock reflectivities were observed. Improvements in the experimental technique include *in situ* temporal calibration of each streaked image, absolute timing of the streak cameras, and improved streak cameras (Sydor streak camera versus Hamamatsu) resulting in improved spatial (80 μm line spread function) and temporal resolution (50 ps) of the streaked images. The Hamamatsu used by Spaulding *et al.* [7] was streak camera model C7700 with an S20 photocathode and an ORCA 2 model C4742-98 CCD. The largest contributing source of error in Spaulding *et al.* may be attributed to the point spread function of the Hamamatsu streak camera [21]. The Sydor streak cameras used in these experiments were Ross 5800's with S20 photocathode and an SI-800 TE cooled camera with E2V CCD. Spaulding *et al.* also used a calibration relative to quartz as well as an absolute tungsten lamp calibration; however, the quartz data in

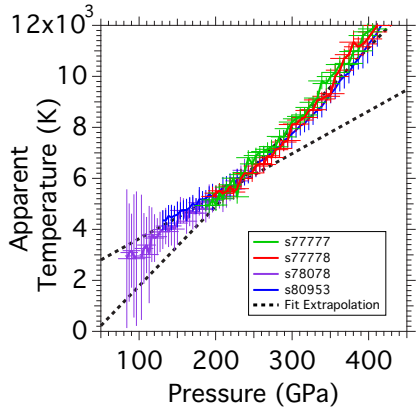

FIG. 6. The observed thermal temperature as a function of pressure for four experiments is shown as the green, red, purple, and blue lines. The two-segment fit is shown as the black line and the extrapolation of each segment is shown as the black dashed line.

that study were not collected in the same shot as we have done here.

In the present experiments, a continuous increase in thermal emission as a function of pressure was recorded, with a discontinuous change in slope at 227 (±10) GPa (see Fig. 6). Historically, discontinuities and plateaus in the temperature-pressure Hugoniot have been associated with phase changes [1–3,22]. However, this work does not show signatures of a latent heat (plateau in temperature with decreasing pressure) or superheating (sudden increase in temperature with decaying pressure). We interpret this change in slope to be associated with a transition from a reflective liquid state into a transparent insulating partial melt. Due to the large change in the refractive index of shocked enstatite, Fresnel reflectivity at the leading density jump is sufficient to produce a detectable VISAR signal within the solid phase ($R \sim 0.4\%$). When the solid phase is transparent ($P < P_{\mathrm{melt}}$), the SOP collects radiation from a finite thickness of material behind the shock front, while the VISAR measures the velocity of the refractive index discontinuity associated with the leading density jump (the shock front). The solid phase is optically thin for the time scales of these experiments, supported by our refractive index measurements (Sec.n V). We conclude that the discontinuous change in slope is an optical manifestation of the transition from a reflective to a translucent shock front.

Radiation-hydrocode simulations using the arbitrary Lagrangian-Eulerian hydrocode (CALE) [23] were performed to examine this hypothesis in detail. We simulated the temperature-pressure observation with the assumption that the solid phase remained transparent and the shock-front velocity is measured from the Fresnel reflection. We used a diamond multiphase EOS [24] since a multiphase EOS for $MgSiO_3$ or other silicates is unavailable. We simulated a decaying shock wave in a diamond sample with initial density of 2.6 g/cc in order to probe a region of the melt line where the Clapeyron slope is positive. In these simulations an initial steady 6 Mbar shock is generated within the diamond sample. After 2 ns the drive is terminated, similar to our OMEGA experiments, generating a centered rarefaction wave that overtakes the leading shock wave generating a shock decay rate similar to

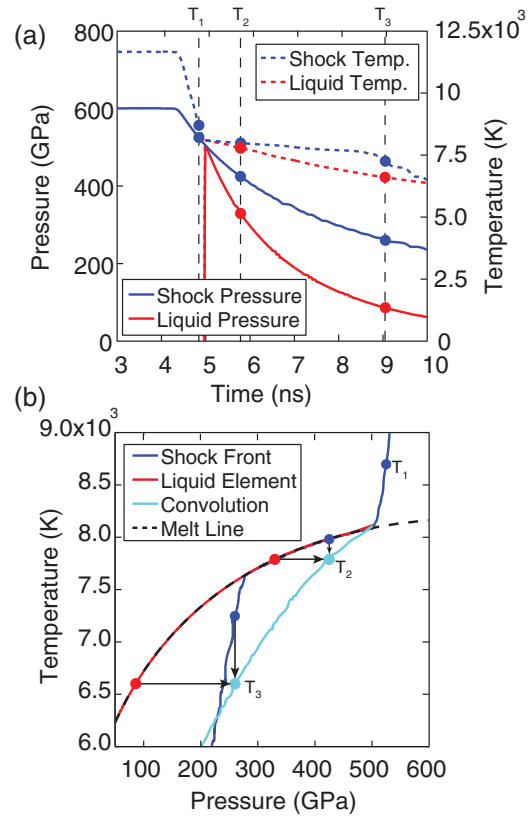

FIG. 7. Radiation hydrocode decaying shock-wave simulations were performed to examine the observed "kink" in thermal emission. (a) The pressure and temperature of the shock front (blue) and last fluid element to remain in the liquid phase (red) are plotted versus time. Three times (T_1, T_2, and T_3) are examined. (b) The shock front (blue), last fluid element (red), and the melt line (black dashed) are shown. The times from (a) illustrates how the shock-front pressure and fluid temperature can be convolved to produce a kink in the thermal emission (cyan line) that occurs at the onset of melt.

our experiments. The results of the hydrocode simulation are shown in Fig. 7(a). The shock-front pressure (blue line) and temperature (blue dashed line) are compared with the pressure (red line) and temperature (red dashed line) of the last element to remain within the solid phase. The vertical dashed lines (T_1, T_2, and T_3) correspond to different snapshots in time.

Figure 7(b) illustrates the temperature-pressure path of the shock front (blue line) and the last fluid element (red line). The melt boundary is shown as the black dashed line. When the decaying shock pressure reaches the melt boundary, the Hugoniot briefly follows the melt boundary due to the latent heat of solidification. The points labeled T_1, T_2, and T_3 in Fig. 7(b) show the correlation between the shock front and the fluid element. For pressure states above the melt boundary, we recover the shock-front temperature and pressure (T_1). After the onset of melt, we observe thermal emission from the bulk and the shock-front pressure. Convolving these observations (T_2 and T_3) gives the cyan trace which shows a change in slope occurs at the onset of melt.

To accurately determine the melt point, we utilized a Levenberg-Marquardt regression routine to fit a continuous piecewise linear function to the apparent shock temperature

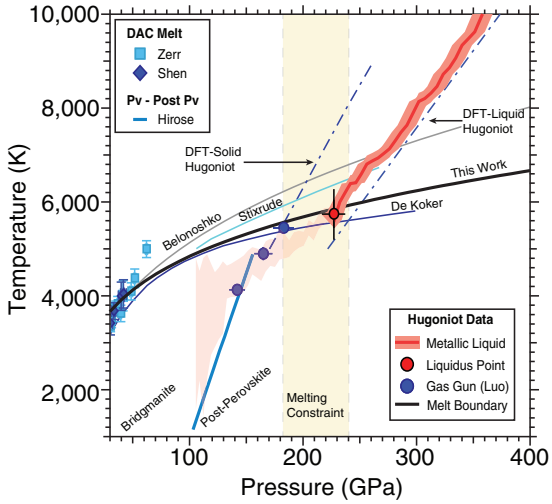

FIG. 8. The continuous measure of the enstatite principal Hugoniot temperature versus pressure is shown as the red shaded region and the onset of melt is indicated by the red point. Our measured temperature pressure path is in good agreement with recent DFT simulations (dot-dashed blue line) [8] for the liquid phase. Our Simon fit for the melt boundary (black line) is compared with predictions [15,26,27] and the measured bridgmanite/post-perovskite phase boundary [28]. The pressure constraints that we place upon melt is shown as the yellow shaded region, indicating that our inferred liquidus melting point is consistent with other observations.

versus shock pressure data. Assuming that the lines intercept at the melt pressure ($P_{\rm melt}$), we fit the data to

$$T = T_1 + s_1 * P \quad \text{for } P < P_{\rm melt} \tag{5}$$

and

$$T = T_1 + (s_1 - s_2) * P_{\rm int} + s_2 * P \quad \text{for } P > P_{\rm melt}, \tag{6}$$

finding the adjustable parameters s_1, s_2, T_1, and $P_{\rm int}$. For the test case shown in Fig. 7, using the localized linear two-segment fit we found the onset of melting to be better than 0.6% in pressure and 0.2% in temperature.

Using this technique on our experimental data shown in Fig. 6, we find that the change in slope is observed at 5745 (±530 K) and 227 (±10) GPa. Using the experimental data from the different techniques, we bound the melt region for $MgSiO_3$ along the enstatite Hugoniot. We find that $P_{\rm melt} > 164$ GPa from refractive index measurements, $P_{\rm melt} > 183$ GPa from gas-gun temperature measurements [11], $P_{\rm melt} > 140$ GPa from gas-gun sound-speed measurements [13], and $P_{\rm melt} < 237$ GPa from our high-pressure sound-speed measurements. These constraints on melting are shown as the yellow region in Fig. 8. Our interpretation of the change in slope in the decaying shock temperature measurements at 227 (±10) GPa representing complete melting (intersection of the Hugoniot with the liquidus) is consistent with these constraints: 183 GPa $< P_{\rm melt} <$ 237 GPa.

The specific heat (C_v) was determined using the procedure outlined by Keeler and Royce [25] and our experimentally determined Grüneisen parameter. At the liquidus, we find the specific heat to be $C_V = 4.3 \pm 0.2 Nk_{\rm B}$ rising to $C_V = 5.7 \pm 0.2 Nk_{\rm B}$ at 17 500 K. Recent DFT simulations of liquid enstatite [15] are in good agreement with these measurements.

VII. IMPLICATIONS

Using our inferred melt data and diamond-anvil-cell melt data above 30 GPa [32,33], we fit the melt boundary of $MgSiO_3$ using Simon's equation: $T_{\rm melt}[{\rm K}] = 2316(\pm 127)[P_{\rm melt} - 20.6(\pm 0.9)]^{0.1769\pm 0.0144}$ where $T_{\rm melt}$ and $P_{\rm melt}$ are the melt temperature and pressure, respectively. The measured melt point and the Simon fit bisect previous theoretical melt predictions (see Fig. 8) [8,15,26,27]. By extrapolating a linear fit to the Luo *et al.* [11] temperature-pressure Hugoniot data to our proposed melt boundary we can constrain the solidus point. We find that $P_{\rm sol} = 190 \pm 30$ GPa and $T_{\rm sol} = 5750 \pm 670$ K.

We also developed a model for the Grüneisen of liquid $MgSiO_3$ over a broad pressure range, based on our measurements, and DFT simulation results [27]. For silicate liquids, the Grüneisen parameter has been shown to increase with density due to a change in oxygen coordination [15]. Once the coordination reaches a maximum, the Grüneisen parameter decreases again as is normally expected at high pressure [34]. The model consists of an exponential form for the low-pressure data bridged through the use of a Gaussian functional form to a high-pressure regime approaching the Al'tshuler criterion

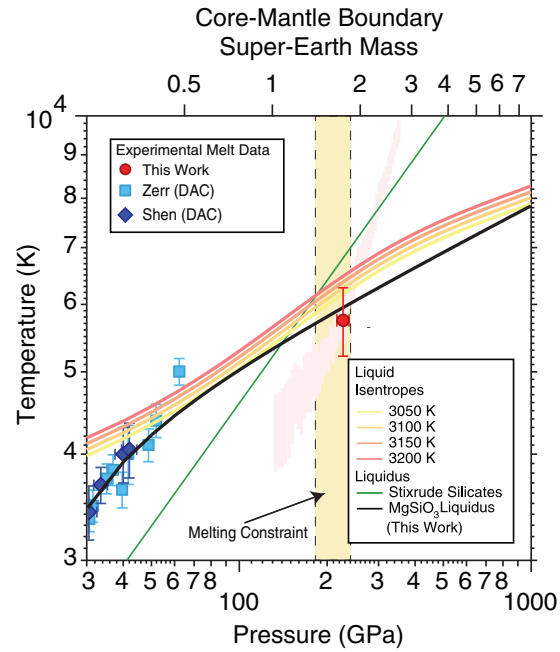

FIG. 9. Liquid silicate pressure-temperature phase diagram compared with core-mantle boundary super-Earth masses [29]. The enstatite Hugoniot melt point (red circle) and the proposed melt boundary (black solid line) extrapolated to high pressure (black line) are compared with previous silicate melt predictions [30] and high-pressure silicate melt data [31]. The pressure constraints that we place upon melt are shown as the yellow shaded region. Predicted liquid isentropes (red-yellow solid lines) for different initial potential temperatures are shown. The mantle adiabats are nearly parallel to the melt boundary, indicating that for a small change in potential energy, super Earths would undergo a drastic rheological transition.

[35]:

$$\Gamma = \Gamma_\infty + (\Gamma_0 - \Gamma_\infty)\left(\frac{\rho_0}{\rho}\right)^\beta + \Gamma_{01} e^{-(\rho-\rho_e)^2/\sigma^2} \quad (7)$$

where $\Gamma_\infty = 0.50$ [35], $\Gamma_0 = 0.3675$, $\Gamma_{01} = 0.65$, $\rho_e = 5.195$ g/cm^3, $\rho_0 = 2.7434$ g/cm^3 are constants and $\beta = 1.0$ and $\sigma = 1707$ g/cm^3 are free fitting parameters.

Using our Grüneisen parameter model and a third-order Birch-Murnaghan equation of state, we compute isentropic temperature profiles for four different isentropes ranging in potential temperature between 3050 and 3200 K (Fig. 9). We find that both the melt curve and the isentropic temperature profiles are shallower than the latest DFT-MD predictions [30] and nearly parallel, consistent with recent thermodynamic modeling of the solid-liquid equilibrium in the MgO-Fe-SiO_2 system [36].

$MgSiO_3$ being a prototypical magma constituent, our measurements up to 384 GPa are directly relevant for the modeling of the structure and evolution of terrestrial super-Earth exoplanets up to three times Earth mass [29] (see Fig. 9). During planetary formation, heating from accretion and radiogenic sources raises the temperature of the planet, potentially resulting in a completely molten mantle. This magma ocean [37] will eventually partially or totally solidify as the planet cools down. Whether the magma ocean solidifies from the top down, from the bottom up, or from a midmantle septum has dramatic implications for the fate of volatiles such as water, with faster cooling planets losing less volatiles through hydrodynamic escape [38].

VIII. CONCLUSION

Our finding of shallow and quasiparallel adiabatic temperature profiles and silicate melt curve (Fig. 9) suggests that complete freezing of a deep silicate magma ocean could occur over a potential temperature range of only a few hundred degrees. Having such a small range of potential temperature that separates a mostly liquid from a mostly solid planet would imply that the planet would solidify rapidly, trapping the water that will be required to facilitate prebiotic chemistry on a potentially habitable super Earth. In addition, in contrast with a recent study suggesting that as planetary mass increases, the melt boundary would increase sufficiently relative to the liquid adiabats such that, at high pressures, the lower mantle would be very difficult to melt completely [30], our shallow melt curve suggests that even large terrestrial exoplanets could have a completely liquid silicate mantle in their early history just after formation.

ACKNOWLEDGMENTS

This work was performed under the auspices of the U.S. Department of Energy by Lawrence Livermore National Laboratory under Contract No. DE-AC52-07NA27344. The authors would like to recognize the staff of the Omega Laser Facility, the target fabrication efforts of Carol Davis and Antonio Correa-Barrios, and Dr. Michail Petaev for electron microprobe measurements. The authors declare that they have no competing financial interests.

[1] D. G. Hicks, T. R. Boehly, J. H. Eggert, J. E. Miller, P. M. Celliers, and G. W. Collins, Phys. Rev. Lett. **97**, 025502 (2006).
[2] M. Millot, N. Dubrovinskaia, A. Černok, S. Blaha, L. Dubrovinsky, D. G. Braun, P. M. Celliers, G. W. Collins, J. H. Eggert, and R. Jeanloz, Science **347**, 418 (2015).
[3] R. S. McWilliams, D. K. Spaulding, J. H. Eggert, P. M. Celliers, D. G. Hicks, R. F. Smith, G. W. Collins, and R. Jeanloz, Science **338**, 1330 (2012).
[4] K. Miyanishi, Y. Tange, N. Ozaki, T. Kimura, T. Sano, Y. Sakawa, T. Tsuchiya, and R. Kodama, Phys. Rev. E **92**, 023103 (2015).
[5] R. M. Bolis, G. Morard, T. Vinci, A. Ravasio, E. Bambrink, M. Guarguaglini, M. Koenig, R. Musella, F. Remus, J. Bouchet, N. Ozaki, K. Miyanishi, T. Sekine, Y. Sakawa, T. Sano, R. Kodama, F. Guyot, and A. Benuzzi-Mounaix, Geophys. Res. Lett. **43**, 9475 (2016).
[6] J. L. Mosenfelder, P. D. Asimow, D. J. Frost, D. C. Rubie, and T. J. Ahrens, J. Geophys. Res.: Earth Surf. **114**, B01203 (2009).
[7] D. K. Spaulding, R. S. McWilliams, R. Jeanloz, J. H. Eggert, P. M. Celliers, D. G. Hicks, G. W. Collins, and R. F. Smith, Phys. Rev. Lett. **108**, 065701 (2012).
[8] B. Militzer, High Energy Density Phys. **9**, 152 (2013).
[9] M. D. Knudson and M. P. Desjarlais, Phys. Rev. B **88**, 184107 (2013).
[10] D. E. Fratanduono, D. H. Munro, P. M. Celliers, and G. W. Collins, J. Appl. Phys. **116**, 033517 (2014).
[11] S.-N. Luo, J. A. Akins, T. J. Ahrens, and P. D. Asimow, J. Geophys. Res.: Earth Surf. **109** (2004).
[12] J. A. Akins, S.-N. Luo, P. D. Asimow, and T. J. Ahrens, Geophys. Res. Lett. **31**, L14612 (2004).
[13] Z. Gong, H. Xie, H. Huo, F. Jing, J. Guo, and J. Xu, Chin. Sci. Bull. **45**, 921 (1999).
[14] M. Murakami, Y. Ohishi, N. Hirao, and K. Hirose, Nature (London) **485**, 90 (2012).
[15] N. De Koker and L. Stixrude, Geophys. J. Int. **178**, 162 (2009).
[16] Z. Zhang, L. Stixrude, and J. Brodholt, Earth Planet. Sci. Lett. **379**, 1 (2013).
[17] S. Brygoo, M. Millot, P. Loubeyre, A. E. Lazicki, S. Hamel, T. Qi, P. M. Celliers, F. Coppari, J. H. Eggert, D. E. Fratanduono, D. G. Hicks, J. R. Rygg, R. F. Smith, D. C. Swift, G. W. Collins, and R. Jeanloz, J. Appl. Phys. **118**, 195901 (2015).
[18] R. G. McQueen, S. P. Marsh, and J. N. Fritz, J. Geophys. Res. **72**, 4999 (1967).
[19] P. M. Celliers, D. K. Bradley, G. W. Collins, D. G. Hicks, T. R. Boehly, and W. J. Armstrong, Rev. Sci. Instrum. **75**, 4916 (2004).
[20] J. Clerouin, Y. Laudernet, V. Recoules, and S. Mazevet, Phys. Rev. B **72**, 155122 (2005).
[21] R. G. Kraus, S. T. Stewart, D. C. Swift, C. A. Bolme, R. F. Smith, S. Hamel, B. D. Hammel, D. K. Spaulding, D. G. Hicks, J. H. Eggert, and G. W. Collins, J. Geophys. Res.: Planets **117**, E09009 (2012).
[22] J. H. Eggert, D. G. Hicks, P. M. Celliers, D. K. Bradley, R. S. McWilliams, R. Jeanloz, J. E. Miller, T. R. Boehly, and G. W. Collins, Nat. Phys. **6**, 40 (2010).

[23] R. Tipton, R. Managan, and P. Amala, CALE User's Manual, Report, Lawrence Livermore National Laboratory, 2010.
[24] L. X. Benedict, K. P. Driver, S. Hamel, B. Militzer, T. Qi, A. A. Correa, A. Saul, and E. Schwegler, Phys. Rev. B **89**, 224109 (2014).
[25] R. Keeler and E. Royce, in *Physics of High Energy Density*, edited by P. Caldirola and H. Knoepfel (Academic, New York, 1971), Vol. 48, pp. 106–125.
[26] A. B. Belonoshko, N. V. Skorodumova, A. Rosengren, R. Ahuja, B. Johansson, L. Burakovsky, and D. L. Preston, Phys. Rev. Lett. **94**, 195701 (2005).
[27] L. Stixrude and B. Karki, Science **310**, 297 (2005).
[28] K. Hirose, N. Takafuji, N. Sata, and Y. Ohishi, Earth Planet. Sci. Lett. **237**, 239 (2005).
[29] F. W. Wagner, N. Tosi, F. Sohl, H. Rauer, and T. Spohn, Astron. Astrophys. **541**, A103 (2012).
[30] L. Stixrude, Philos. Trans. R. Soc. London, Ser. A **372**, 20130076 (2014).
[31] G. Fiquet, A. L. Auzende, J. Siebert, A. Corgne, H. Bureau, H. Ozawa, and G. Garbarino, Science **329**, 1516 (2010).
[32] A. Zerr and R. Boehler, Science **262**, 553 (1993).
[33] G. Shen and P. Lazor, J. Geophys. Res.: Earth Surf. **100**, 17699 (1995).
[34] O. L. Anderson, *Equations of State of Solids for Geophysics and Ceramic Science (Book 31)* (Oxford University Press, Oxford, 1995).
[35] L. Burakovsky and D. L. Preston, J. Phys. Chem. Solids **65**, 1581 (2004).
[36] C. E. Boukaré, Y. Ricard, and G. Fiquet, J. Geophys. Res.: Earth Surf. **120**, 6085 (2015).
[37] A. N. Halliday, H. Wänke, J. L. Birck, and R. N. Clayton, The Accretion, Composition and Early Differentiation of Mars, *Chronology and Evolution of Mars*, Space Sciences Series of ISSI Vol. 12 (Springer, The Netherlands, 2001), Book section 7, pp. 197–230.
[38] K. Hamano, Y. Abe, and H. Genda, Nature (London) **497**, 607 (2013).